Nonlinear refractive indices in Yb^{3+}-doped and undoped monoclinic double tungstates KRE(WO$_4$)$_2$ where RE = Gd, Y, Yb, Lu

**N. Thilmann · G. Strömqvist · M.C. Pujol ·
V. Pasiskevicius · V. Petrov · F. Díaz**

Abstract The linear absorption bandgap in the ultraviolet and the nonlinear index n_2 in near infrared were systematically measured in undoped and Yb^{3+}-doped top-seeded solution-grown monoclinic double-tungstate KRE(WO$_4$)$_2$ (RE = Gd, Y, Yb, Lu) crystals. Anisotropic n_2 nonlinear indices have been determined for $E \parallel N_m$ and $E \parallel N_p$ polarizations with the maximum nonlinear index n_2 observed for the light polarized $E \parallel N_m$. Moreover, the value of the nonlinear response of particular crystals in this family is proportional to the ionic radius of the RE^{3+} ion.

PACS 42.65.An · 42.65.Hw · 42.70.Hj

1 Introduction

Double tungstate and double molybdate crystals with the general formula MRE(XO$_4$)$_2$ (shortly MREX), where M is a monovalent alkali cation, RE is a trivalent cation Y, Yb, La, Gd, Lu, or Bi and X is W or Mo, are currently witnessing an increase of interest as laser host materials [1–6]. In this respect, the monoclinic double tungstates KGdW,

N. Thilmann (✉) · G. Strömqvist · V. Pasiskevicius
Department of Applied Physics, Royal Institute of Technology (KTH), Roslagstullsbacken 21, 10691 Stockholm, Sweden
e-mail: nt@laserphysics.kth.se
Fax: +46-08-55378216

M.C. Pujol · F. Díaz
Física i Cristalografia de Materials i Nanomaterials (FiCMA-FiCNA), Universitat Rovira i Virgili (URV), Campus Sescelades, C/Marcellí Domingo s/n, 43007 Tarragona, Spain

V. Petrov
Max-Born Institute, Max-Born-Strasse 2A, 12489 Berlin, Germany

KYW, KLuW, and KYbW have shown good potential for applications in coherent light sources owing to the high optical quality, relatively large apertures, and good homogeneity of the crystals. These biaxial crystals are characterized by a large anisotropy of linear dielectric, mechanical, and thermal properties [4–6]. Concomitant anisotropy in absorption and emission cross-sections of rare-earth dopant-ions allows for a unique combination of large cross-section and broad bandwidth for electric field direction parallel to the N_m index axis. This feature has been very actively exploited in the case of Yb^{3+}-doped monoclinic double-tungstate hosts, enabling highly efficient diode-pumped tunability laser operation [7–10] or ultrashort pulse generation [11–16]. Most of the femtosecond lasers based on monoclinic Yb^{3+}-doped double tungstates employ a semiconductor saturable absorber mirror for self-starting mode-locking demonstrating pulse-lengths above 100 fs. On the other hand, one of the early diode-pumped femtosecond Yb:KYW lasers employed Kerr-lens mode-locking and demonstrated pulses of 71 fs and tunability [15]. In that work the nonlinear index coefficient $n_2 = 8.7 \times 10^{-16}$ cm^2/W was reported with the reference to the earlier measurement in [17]. However, in [17] the measurement at 1.08 μm wavelength was performed for a polarization that apparently did not correspond to one of the refractive index axes in this material. Moreover, comparison of the laser performance in [15] with simulations in [17] indicate that the nonlinear index coefficient is probably larger. Indeed, later measurements of n_2 at 790 nm for the light polarization $E \parallel N_m$ show substantially larger values, e.g., $n_2 = 21 \times 10^{-16}$ cm^2/W for KYW [18]. In the same work [18], it was reported that the nonlinear index coefficient is isotropic for polarizations $E \parallel N_m$ and $E \parallel N_p$ within the uncertainty of the measurements. This stands in contrast to the measurements in Yb:KGdW [19], where anisotropic and virtually dispersionless Kerr response has been found

in the near infrared. It should be noted that our previous investigations of n_2 in disordered tetragonal NaTW family of isomorphs showed large and isotropic nonlinear index coefficients [20].

The above mentioned uncertainty in the nonlinear index measurement in monoclinic double tungstates and also the lack of measurements in a new member of this isostructural group, namely KLuW, prompted us to systematically measure nonlinear index coefficient in undoped and Yb^{3+}-doped crystals for different light polarizations.

2 Material growth and sample preparation

Double tungstates show polymorphism with temperature, but the low-temperature monoclinic phase can be obtained by high-temperature solution growth methods, specifically here the top-seeded solution-growth slow-cooling method (TSSG-SC) using $K_2W_2O_7$ solvent [21]. The solution composition is about 12/88 mol.% solute/solvent. The bulk crystals are grown in cylindrical tubular furnaces, using Pt crucibles. The starting precursor oxides are K_2CO_3, WO_3, and RE_2O_3 (RE = Gd, Y, Yb, Lu) with 99.9% purity. A KREW seed (RE = Gd, Y, Yb, and Lu) oriented along the **b** crystallographic axis is attached to a Pt holder rotating at 40–60 rpm. The temperature gradient in the solution is about 1 K/cm in the vertical and radial directions with the bottom and walls being hotter. The growth occurs as a result of supersaturation when cooling below the saturation temperature. The saturation temperature has been separately determined for each solute and ranged between 1146 K for KLuW and 1203 K for KGdW. The usual cooling rate during growth varies between 0.05 and 0.3 K/h, depending on the compound itself as well as the doping. Finally, the grown crystals are removed slowly from the solution and cooled at a rate of 15–25 K/h, slightly above the solution surface but inside the furnace. The Yb^{3+}-doped samples were grown with a nominal 5 at.% Yb in solution in relation to the RE.

The ordered double tungstates KREW, as they belong to the monoclinic system, (space group $C2/c$, $2/m$ point group) are optically biaxial. The dielectric tensor coordinate frame of these materials has been described in the literature [4, 5, 22, 23]. It is defined by one main index axis, labeled N_p, parallel to the **b** crystallographic axis and the other two index axes (N_g and N_m) located in the **a**–**c** crystallographic {010} plane. When positive **b** is pointing to the observer, N_g is rotated by an angle κ in clockwise direction to the **c** crystallographic axis, κ being 21.5º, 18.5º, 19º, and 18.5º for KGdW, KYW, KYbW, and KLuW, respectively. The axis notations follow the $N_p < N_m < N_g$ relation for the corresponding principal refractive indices. The n_2 coefficient was measured in the orthogonal frame of the optical indicatrix, which, as the **abc** frame, is right handed. The symmetry
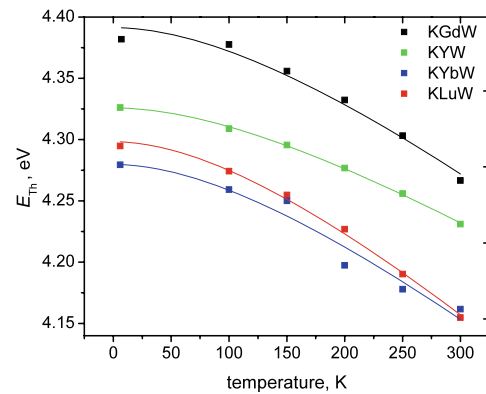

Fig. 1 Threshold energy E_{th} (*filled squares*) and polynomial fit (*solid lines*)

of the $\chi^{(3)}$ tensor differs from the crystallographic symmetry but the dielectric axes are still symmetry elements corresponding to maximum n_2 values [24] which justifies the selection of this reporting frame.

In the present work, the samples have been cut and polished perpendicular to the N_g index axis, in order to access the axes N_m and N_p. For measurements of the linear fundamental absorption edge the samples were polished down to thickness of 70 μm, while the thickness of all samples used to measure the n_2 index was about 1 mm.

3 Experimental results and discussion

To obtain the bandgap energies E_{gap}, the optical absorption spectra in the ultraviolet region between 3.47 eV (357 nm) and 4.46 eV (278 nm) were recorded. The measurements were carried out in a temperature range of 6–300 K in a Varian Cary 500 spectrometer. Sample cooling for the low temperature measurements was accomplished by Oxford Instruments cryostat (SU 12 model) with close-cycle helium gas flow. From an extrapolation of the linear part of an $(\alpha E)^2$ versus E plot, where α is the optical density and E is the photon energy, one can obtain the values of the threshold energy E_{th} which correspond to the bandgap energies E_{gap} assuming that the ultraviolet absorption is due to direct dipole-allowed interband transitions. The obtained values are shown in Table 1 together with the data of KGdW from [25]. The data points in Fig. 1 show the measured temperature-dependence of the bandgap in the different crystals. The thermal bandgap coefficients $\partial E_{gap}/\partial T$ estimated from the high-temperature side of the dependencies in Fig. 1 are -5.37×10^{-4}, -4.2×10^{-4}, -6.29×10^{-4}, and -5.36×10^{-4} eV/K for KGdW, KYW, KLuW, and KYbW, respectively.

The nonlinear refractive index n_2 was measured using the z-scan method introduced by Sheik-Bahae et al. [26]. This technique allows determining sign and magnitude of

Table 1 The extracted threshold energies E_{th} for different temperatures T

	E_{th} for $T = 6$ K [eV]	E_{th} for $T = 100$ K [eV]	E_{th} for $T = 150$ K [eV]	E_{th} for $T = 200$ K [eV]	E_{th} for $T = 250$ K [eV]	E_{th} for $T = 300$ K [eV]
KLuW	4.30	4.28	4.26	4.23	4.20	4.16
KYbW	4.29	4.26	4.26	4.20	4.18	4.15
KYW	4.33	4.31	4.30	4.28	4.26	4.24
KGdW	4.38	4.38	4.36	4.34	4.31	4.27

the nonlinear refractive index n_2 in a single measurement using a single beam. The method is based on the intensity dependency of the phase shift introduced by a change of the refractive index. This leads to a variation in the transmitted power through a far-field aperture while the sample is translated along the z-axis. The refractive index n can be written as $n = n_1 + n_2 I$, where I is the intensity of the laser beam inside the crystal and n_1 and n_2 are the linear and nonlinear refractive indices, respectively. Under the assumption of a Gaussian beam and a small sample length L (shorter than the Rayleigh length z_0 of the probe beam), the phase shift at beam focus can be described by

$$\Delta\Phi_0(t) = \frac{n_2 I_0(t) L_{eff} 2\pi}{\lambda}, \tag{1}$$

where, for insignificant linear optical losses, $L_{eff} \approx L$, and $I_0(t)$ is the time-dependent intensity at the focus. As the laser used was pulsed, the time averaged refractive index change

$$\langle \Delta n_0(t) \rangle = \frac{n_2 I_0}{\sqrt{2}} \tag{2}$$

was measured. Here I_0 is the peak intensity at the focus. This change in the refractive index introduces an intensity modulation of the light that is transmitted through the far-field aperture due to focusing and defocusing introduced by the sample. The amount of focusing and defocusing itself depends on the position of the sample with respect to the focus of the incident beam, i.e., the sample position along the z-axis. During the scan the transmittance T is described by

$$T(z, \Delta\Phi_0) \approx 1 - \frac{4\Delta\Phi_0 x}{(x^2 + 9)(x^2 + 1)}; \quad \text{with } x = \frac{z}{z_0}. \tag{3}$$

Using (3) one can calculate the extrema (peak and valley) of the transmittance and find the difference between the peak and valley transmittance to be $\Delta T_{pv} \approx 0.406(1 - S)^{0.25}|\langle \Delta\Phi_0(t) \rangle|$, where S is the linear transmittance of the far-field aperture. By using (1) to (3), the nonlinear refrac-

tive index can be expressed by:

$$n_2 = \sqrt{2}\frac{\Delta\Phi_0}{I_0 L}\frac{\lambda}{2\pi} \tag{4a}$$

$$= \sqrt{2}\frac{\Delta T_{pv}}{0.406(1 - S)^{0.25} I_0 L}\frac{\lambda}{2\pi}. \tag{4b}$$

Besides the intensity-dependent nonlinear refractive index, other effects can, depending on the z-position of the sample, lead to changes in the power transmitted through the far-field aperture. This can be a misalignment or a nonparallelism of the crystal surfaces introducing a tilt of the beam, and therefore making the power transmitted through the far-field aperture depend on the beam origin, i.e., the sample position. Further, occurrence of the intensity-dependent two-photon absorption (TPA) influences the total intensity after the crystal, and therefore modifies the power transmitted through the far-field aperture. To avoid the tilt of the beam, special care was taken during sample alignment and monitoring of the TPA allowed to correct the measurement [25].

Pulses derived from a tunable picosecond Ti:sapphire regenerative amplifier were used for the measurements in this work. The central wavelength of the linearly polarized pulses was 819 nm with a pulse length of 4 ps (intensity FWHM) and a repetition rate of 1 kHz. The pump photon energy was chosen such that it was substantially moved away from the resonant transitions of the Yb^{3+} dopant but was close enough to the 1 µm wavelength region where laser operation in these materials is normally obtained. After reduction of the diameter with a reflective telescope, the beam was focused by a 150 mm focal length lens yielding a spot size of $\sim$25 µm ($1/e^2$ intensity radius) measured by the knife edge technique. The pulse length and pulse energy were chosen after initially determining that material modification occurs at peak intensities above 98 GW/cm^2 for 2 ps pulses. The pulse length of 4 ps was an optimum that allowed keeping a relatively high average power for the far-field measurements and, at the same time, operating safely below the optical damage threshold. The sample was mounted on a motorized computer-controlled translation stage with a travel range of about $\pm$18 mm along the z-axis. A CaF$_2$ crystal beam splitter after the sample allowed monitoring of the total transmitted near field intensity by a photodiode (PD) to

Table 2 The measured nonlinear indices for the two orthogonal polarizations $E \| N_m$ and $E \| N_p$ and the anisotropy of the nonlinear index coefficient

Crystal	Dopant	$n_2 E \| N_m$ [10^{-16} cm^2 W^{-1}]	$n_2 E \| N_p$ [10^{-16} cm^2 W^{-1}]	$n_2 \| N_m - n_2 \| N_p$ [10^{-16} cm^2 W^{-1}]
KLuW	–	23	17	6
KLuW	Yb (5 at.%)	22	19	3
KYbW	–	23	17	6
KYW	–	24	15	9
KYW	Yb (5 at.%)	19	15	4
KGdW	–	25	15	10
KGdW	Yb (5 at.%)	26	17	9

detect TPA. The far-field iris aperture was placed ∼60 cm behind the sample followed by a power meter. Prior to the actual scanning measurement with the crystal away from focus, the power in front and directly behind the crystal was measured. The average incident power used in these measurements was found to be 4.14 mW (4.14 μJ per pulse). The linear transmission of the samples was about 80% and is well accounted for by the Fresnel reflection losses. For each measurement the transmitted power through the far-field aperture was 0.6 mW, which corresponds to the aperture transmission $S \approx 0.18$. The z-scan itself was carried out using varying step sizes from 0.25–3 mm with smallest steps near the focus. For each sample we measured z-scan traces for laser polarizations $E \| N_m$ and $E \| N_p$.

Prior to fitting the experimental traces with (3), the far-field transmittance signal was scaled by the signal from the PD to correct for the possible occurrence of TPA [25]. In fact, the TPA was very small in all samples with a maximum transmission modulation of ∼3% in KLuW. The nonlinear refractive indices were calculated using (4a). Here the intensity at the focus I_0 was calculated using the measured incident power corrected by a single Fresnel reflection on the first surface of the crystal. Beam profile and pulse shape were assumed to be Gaussian, and the spot size at the focus could be ascertained using the Rayleigh length z_0 from (3) fitting procedure.

Figure 2 shows the experimental z-scan traces of all crystals together with the fitted curves. The extracted values of the nonlinear index coefficient are summarized in Table 2 for both polarizations. Several observations can be made from the experimental data. First, the values of nonlinear refractive indices are similar to those reported in Yb:KGdW in [19] and also in tetragonal double tungstates such as NaLuW [20]. Second, there is anisotropy in n_2; the values for the light polarization $E \| N_m$ are always larger than the values for the polarization $E \| N_p$. This is beneficial because larger absorption and emission cross-sections are observed with $E \| N_m$. Our measurement is again in agreement with previous observations in monoclinic Yb:KGdW [19]. Third, this anisotropy in the nonlinear refractive index is reduced in all investigated crystals containing Yb^{3+} doping.

Fourth, in terms of increasing the nonlinear index coefficient, the investigated double tungstates can be ranked as follows: KLuW, KYbW, KYW, KGdW. This is also the order in which the anisotropy of the nonlinear response increases.

The larger values of n_2 for the polarization $E \| N_m$ are expected if we assume validity of the semiempirical Miller's rule and considering that this polarization also corresponds to the largest linear index. For this polarization the electric field lies in the (**a–c**) crystallographic plane of interconnected REO$_8$ and KO$_{12}$ polyhedra alternating with wolframate chains [6]. The investigated compounds differ only by the RE^{3+} cation, which is also the site for substitution by Yb^{3+} doping. So in order to understand different n_2 values in the investigated materials, we look for a correlation between the nonlinear response and the RE^{3+} cation polarizability. The linear ionic polarizability of RE^{3+} ions increases with the ionic radius [27–29]. Figure 3 shows the dependence of the n_2 for the polarization $E \| N_m$ as a function of RE^{3+} ionic radius revealing an approximately linearly proportional increase of the nonlinear response with the ionic radius. However, we should consider that the nonlinear response is also dependent on bond polarizability and structural distortion in REO$_8$ groups. The structural distortion of REO$_8$ groups in monoclinic double-tungstates tends to decrease with the RE^{3+} ionic radius [4–6]. This bond-symmetrizing effect can partly counteract to the effect of increased ionic polarizability.

4 Conclusions

In this work, we systematically investigated the nonlinear index coefficient n_2 in undoped and Yb^{3+}-doped TSSG-SC grown monoclinic double tungstate isomorphs KGdW, KYW, KYbW, and KLuW with good potential for ultrashort pulse lasers. The values of n_2 in all compounds are similar to those previously reported in Yb:KGdW although there is a trend for n_2 to increase for larger rare-earth ion radii. Moreover, the anisotropy of n_2 is confirmed with the larger value obtained for the light polarization parallel to the N_m-axis.
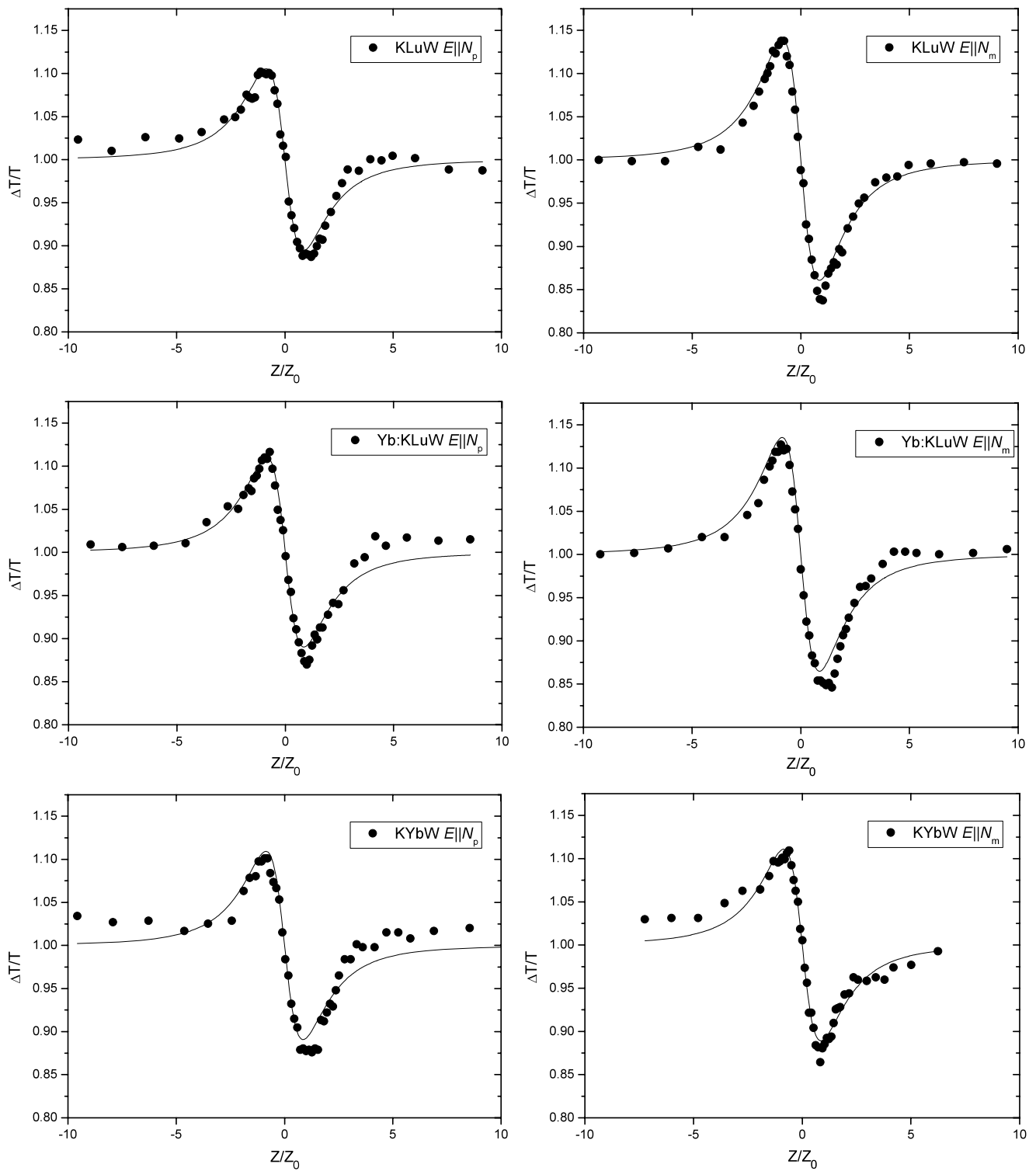
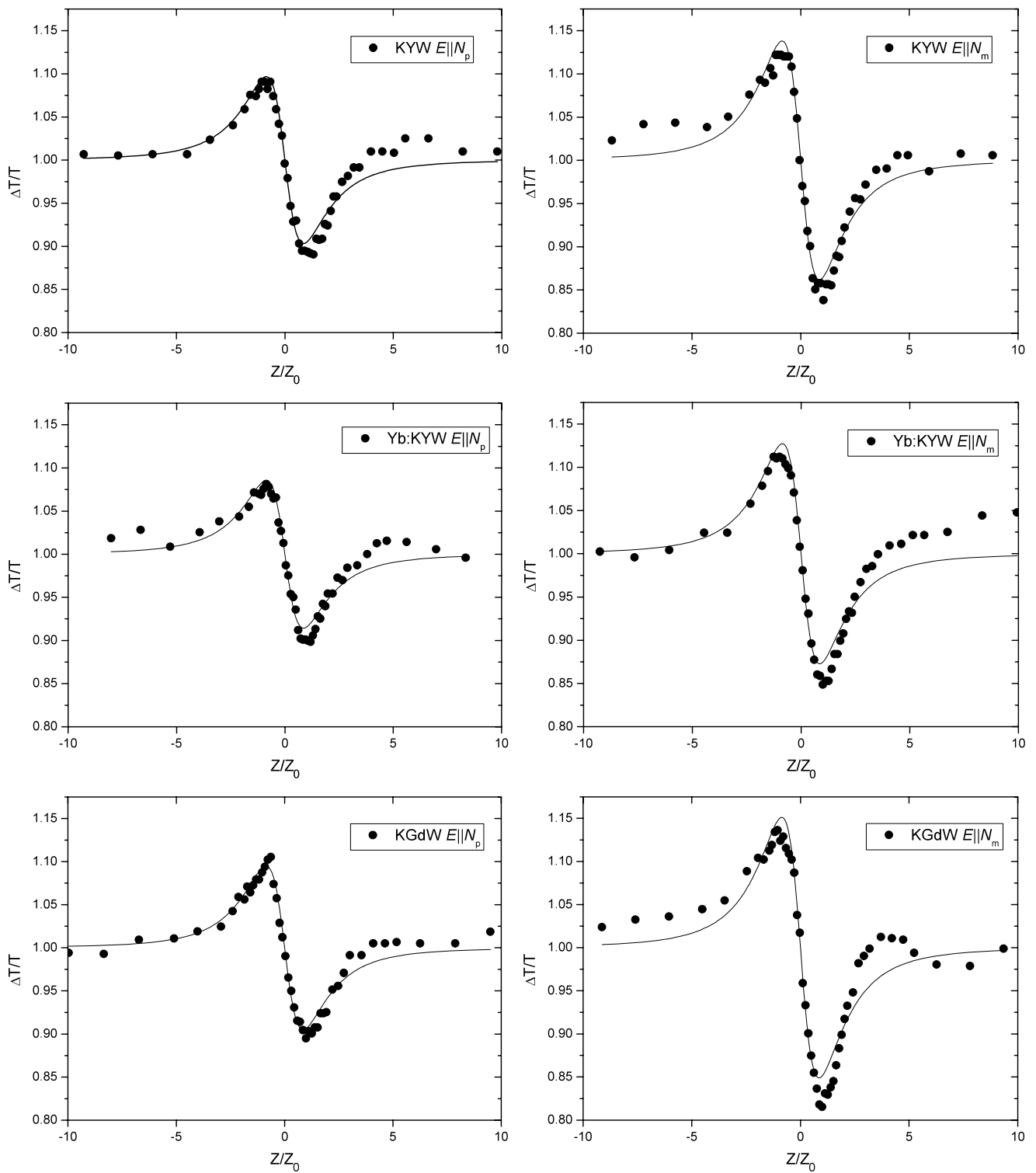**Fig. 2** Experimental far-field *z*-scan results (*points*) and theoretical fit (*solid line*)
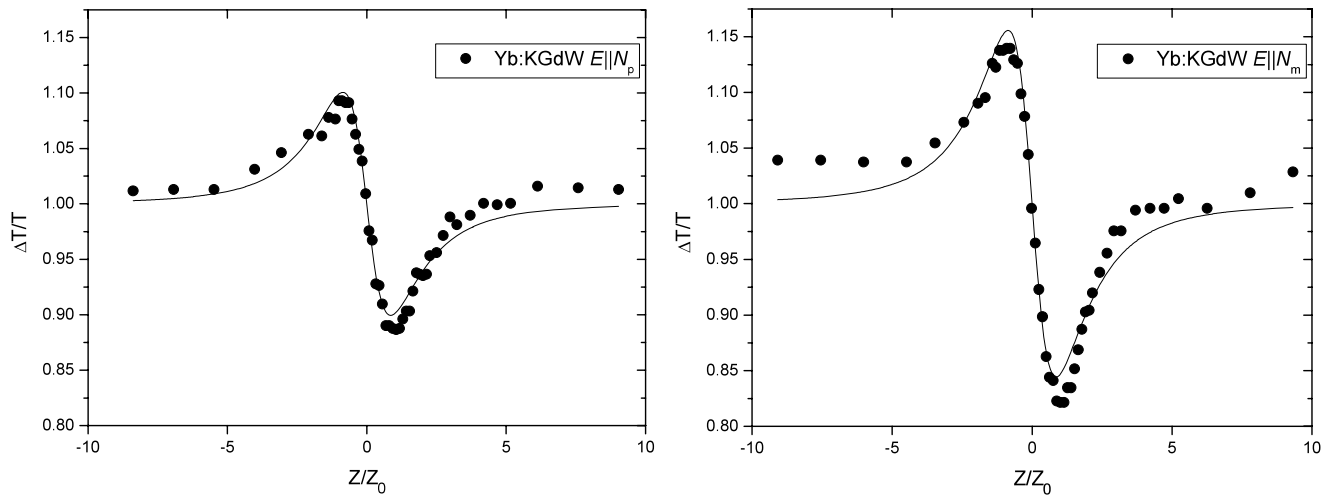
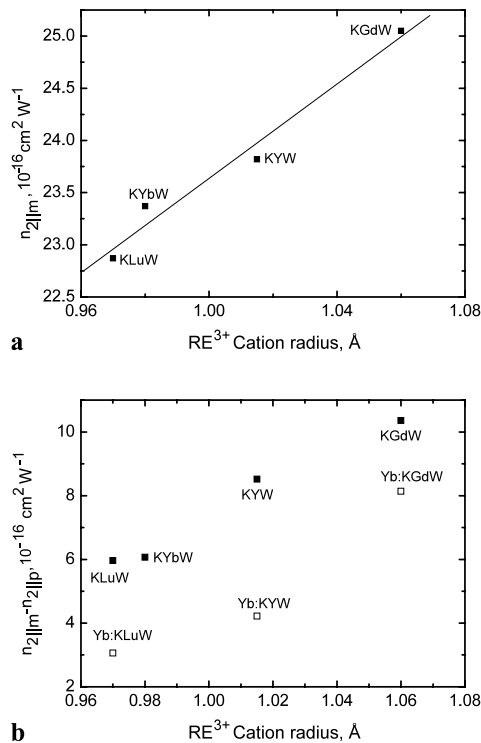**Fig. 2** (*Continued*)

Fig. 2 (*Continued*)

Fig. 3 (**a**) Nonlinear index coefficient for undoped double tungstates as a function of RE^{3+} cation radius (*solid squares*) and linear fit to the experimental points (*solid line*). (**b**) Birefringence of the nonlinear index coefficient for undoped (*solid squares*) and 5 at.% Yb^{3+}-doped (*open squares*) double tungstates as a function of RE^{3+} cation radius

References

1. A. Brenier, G. Boulon, Europhys. Lett. **55**, 647 (2001)
2. A.A. Kaminskii, Laser Photonics. Rev. **1**, 93 (2007)
3. X. Mateos, V. Petrov, M. Aguiló, R.M. Solé, J. Gavaldà, J. Massons, F. Díaz, U. Griebner, IEEE J. Quantum Electron. **40**, 1056 (2004)
4. V. Petrov, M. Cinta Pujol, X. Mateos, Ò. Silvestre, S. Rivier, M. Aguiló, R.M. Solé, J. Liu, U. Griebner, F. Díaz, Laser Photonics Rev. **1**, 179 (2007)
5. M.C. Pujol, M.A. Bursukova, F. Güell, X. Mateos, R. Solé, J. Gavaldà, M. Aguiló, J. Massons, F. Díaz, P. Klopp, U. Griebner, V. Petrov, Phys. Rev. B **65**, 165121 (2002)
6. M.C. Pujol, R. Solé, J. Massons, J. Gavaldà, X. Solans, C. Zaldo, F. Díaz, M. Aguiló, J. Appl. Crystallogr. **34**, 1 (2001)
7. J.E. Hellström, S. Bjurshagen, V. Pasiskevicius, J. Liu, V. Petrov, U. Griebner, Appl. Phys. B, Lasers Opt. **83**, 235 (2006)
8. B. Jacobsson, J.E. Hellström, V. Pasiskevicius, F. Laurell, Opt. Express **15**, 1003 (2007)
9. A.A. Lagatsky, N.V. Kuleshov, V.P. Mikhailov, Opt. Commun. **165**, 71 (1999)
10. J. Liu, U. Griebner, V. Petrov, H. Zhang, J. Zhang, J. Wang, Opt. Lett. **30**, 2427 (2005)
11. F. Brunner, T. Südmeyer, E. Innerhofer, F. Morier-Genoud, R. Paschotta, V.E. Kisel, V.G. Shcherbitsky, N.V. Kuleshov, J. Gao, K. Contag, A. Giesen, U. Keller, Opt. Lett. **27**, 1162 (2002)
12. U. Griebner, S. Rivier, V. Petrov, M. Zorn, G. Erbert, M. Weyers, X. Mateos, M. Aguiló, J. Massons, F. Díaz, Opt. Express **13**, 3465 (2005)
13. G.R. Holtom, Opt. Lett. **31**, 2719 (2006)
14. P. Klopp, V. Petrov, U. Griebner, G. Erbert, Opt. Express **10**, 108 (2002)
15. H. Liu, J. Nees, G. Mourou, Opt. Lett. **26**, 1723 (2001)
16. A. Major, V. Barzda, P.A.E. Piunno, S. Musikhin, U.J. Krull, Opt. Express **14**, 5285 (2006)
17. K.V. Yumashev, N.N. Posnov, P.V. Prokoshin, V.L. Kalashnikov, F. Mejid, I.G. Poloyko, V.P. Mikhailov, V.P. Kozich, Opt. Quantum Electron. **32**, 43 (2000)
18. A.I. Vodchits, V.P. Kozich, V.A. Orlovich, P.A. Apanasevich, Opt. Commun. **263**, 304 (2006)
19. A. Major, I. Nikolakakos, J.S. Aitchison, A.I. Ferguson, N. Langford, P.W. Smith, Appl. Phys. B, Lasers Opt. **77**, 433 (2003)

20. A. García-Cortés, M.D. Serrano, C. Zaldo, C. Cascales, G. Strömqvist, V. Pasiskevicius, Appl. Phys. B, Lasers Opt. **91**, 507 (2008)

21. R. Solé, V. Nikolov, X. Ruiz, J. Gavaldà, X. Solans, M. Aguiló, F. Díaz, J. Cryst. Growth **169**, 600 (1996)

22. X. Mateos, R. Solé, J. Gavaldá, M. Aguiló, J. Massons, F. Díaz, Opt. Mater. **28**, 423 (2006)

23. M.C. Pujol, M. Rico, C. Zaldo, R. Solé, V. Nikolov, X. Solans, M. Aguiló, F. Díaz, Appl. Phys. B, Lasers Opt. **68**, 187 (1999)

24. A.V. Mikhailov, I.V. Mochalov, Opt. Spektrosk. **67**, 734 (1989)

25. M.C. Pujol, R. Solé, J. Gavaldà, J. Massons, M. Aguiló, F. Díaz, V. Nikolov, C. Zaldo, J. Mater. Res. **14**, 3739 (1999)

26. M. Sheik-Bahae, A.A. Said, T.H. Wei, D.J. Hagan, E.W. Vanstryland, IEEE J. Quantum Electron. **26**, 760 (1990)

27. N.W. Grimes, R.W. Grimes, J. Phys., Condens. Matter **10**, 3029 (1998)

28. C. Clavaguéra, J.P. Dognon, Chem. Phys. **311**, 169 (2005)

29. D. Xue, K. Betzler, H. Hesse, J. Phys., Condens. Matter **12**, 3113 (2000)